ACS NANO
Cite This: ACS Nano XXXX, XXX, XXX−XXX
www.acsnano.org

ARTICLE

Revealing the Effects of Electrode Crystallographic Orientation on Battery Electrochemistry *via* the Anisotropic Lithiation and Sodiation of ReS_2

Qianqian Li,[†,‡,∥] Yaobin Xu,[†,‡] Zhenpeng Yao,[†,¶] Joohoon Kang,[†] Xiaolong Liu,[†,§] Chris Wolverton,[†] Mark C. Hersam,[†,§,⊥,#] Jinsong Wu,[*,†,‡] and Vinayak P. Dravid[*,†,‡]

[†]Department of Materials Science and Engineering, [‡]The NU*ANCE* Center, [§]Applied Physics Graduate Program, [⊥]Department of Chemistry, and [#]Department of Electrical Engineering and Computer Science, Northwestern University, Evanston, Illinois 60208, United States

[∥]Materials Genome Institute, Shanghai University, Shanghai 200444, People's Republic of China

Supporting Information

ABSTRACT: **The crystallographic orientation of battery electrode materials can significantly impact electrochemical performance, such as rate capability and cycling stability. Among the layered transition metal dichalcogenides, rhenium disulfide (ReS_2) has the largest anisotropic ratio between the two main axes in addition to exceptionally weak interlayer coupling, which serves as an ideal system to observe and analyze anisotropy of electrochemical phenomena. Here, we report anisotropic lithiation and sodiation of exfoliated ReS_2 at atomic resolution using *in situ* transmission electron microscopy. These results reveal the role of crystallographic orientation and anisotropy on battery electrode electrochemistry. Complemented with density functional theory calculations, the lithiation of ReS_2 is found to begin with intercalation of Li-ions, followed by a conversion reaction that results in Re nanoparticles and Li_2S nanocrystals. The reaction speed is highly anisotropic, occurring faster along the in-plane ReS_2 layer than along the out-of-plane direction. Sodiation of ReS_2 is found to proceed similarly to lithiation, although the intercalation step is relatively quicker. Furthermore, the microstructure and morphology of the reaction products after lithiation/sodiation show clear anisotropy along the in-plane and out-of-plane directions. These results suggest that crystallographic orientation in highly anisotropic electrode materials can be exploited as a design parameter to improve battery electrochemical performance.**

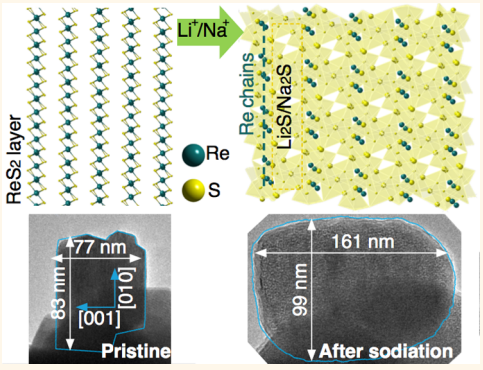

KEYWORDS: *reaction mechanism of lithium/sodium-ion battery, 2D transition metal dichalcogenides, anisotropic lithiation and sodiation, ReS_2, in situ transmission electron microscopy*

The development of lithium- and sodium-ion batteries with high power density and rate capability is essential for many large-scale applications, such as electric vehicles and grid-level storage for renewable energy. The crystalline structure and composition of electrode materials play a critical role in determining the electrochemical performance of lithium- and sodium-ion batteries. In many cases, it has also been observed that electrochemical performance is influenced by the crystallographic orientation of the electrode materials. For instance, anatase TiO_2 crystals that present (001) surface facets possess an enhanced lithiation performance compared to randomly oriented crystals, which can be attributed to more favorable Li insertion and facile Li diffusion along the [001] direction.[1−3] While it may come across as intuitively obvious, there are surprisingly no direct observations or any quantitative assessment of anisotropy of lithiation/sodiation in lithium/sodium electrochemical charge storage systems.

Layered transition metal dichalcogenides (TMDs) have been applied in energy storage due to their high theoretical capacity and layered structure.[4−8] Especially when used as anode materials in rechargeable batteries, TMDs exhibit improved electrochemical performance in comparison to commercial graphite materials (372 mAh g^{-1}).[5,6] In these anisotropic materials, crystallographic

Received: March 23, 2018
Accepted: July 9, 2018
Published: July 9, 2018

DOI: 10.1021/acsnano.8b02203
ACS Nano XXXX, XXX, XXX−XXX

orientation has been found to affect electrochemical performance, such as vertically oriented rhenium disulfide (ReS_2), showing enhanced cycling stability compared to orthogonal orientations.[9,10]

ReS_2 (with a space group of $P\bar{1}$ and unit cell parameters of a = 6.352 Å, b = 6.446 Å, c = 12.779 Å, α = 91.51°, β = 105.17°, and γ = 118.97°) has many characteristics including the following: (1) ReS_2 shows an unusual distorted 1T structure with random stacking and thus an in-plane anisotropy in physical properties;[11] (2) ReS_2 is characterized to be direct bandgap in both bulk materials and monolayers;[12,13] (3) ReS_2 exhibits the greatest anisotropic ratio along the two in-plane axes among the experimentally investigated 2D layered materials;[14] (4) ReS_2 has an exceptionally weak van der Waals interlayer coupling of ~18 meV per unit cell (for comparison, the interlayer coupling is 460 meV for MoS_2).[15] This combination of attributes provides opportunities for Li^+ and Na^+ to efficiently diffuse inside of the ReS_2 structure, with great potential application in high current density rechargeable batteries. ReS_2 has a theoretical capacity of 430 mA h g^{-1} with 4 mol of Li^+ ion insertion per formula. The storage capacity can be improved to over 1000 mA h g^{-1} by coupling with graphene[9−16] or carbon nanotubes.[17] The relatively large interlayer spacing in ReS_2 also allows lithium-ion diffusion without significant volume expansion.[9] However, relatively little work has explored the atomic-scale reaction mechanism and microstructural evolution of ReS_2 during lithiation and sodiation, suggesting the need for a combined *in situ* transmission electron microscopy (TEM) and density functional theory (DFT) approach, which has been previously employed to explore intercalation and conversion reaction processes in other battery electrode materials.[8,18−20]

In this work, we have employed *in situ* TEM combined with DFT calculations to uncover the structure and dynamics of ReS_2 lithiation and sodiation in real time, thus elucidating anisotropic effects (such as volumetric expansion and reaction speed) and reaction products. We find that the direction with the largest expansion is along the out-of-plane [001] axis upon the lithiation and sodiation of ReS_2. Meanwhile, the reaction speed is observed to be the fastest along the in-plane direction. This study thus suggests strategies for exploiting crystallographic orientation to optimize the electrochemical performance of ReS_2 in rechargeable battery applications.

RESULTS AND DISCUSSION

In-situ TEM allows the observation of lithiation and sodiation of ReS_2 along different crystallographic orientations. Figure 1 and Figures S1−S3 show the directional lithiation of ReS_2 along different crystallographic orientations. In Figure 1(a), while the ReS_2 crystal marked by letter "c" is oriented along the [001] axis, the other ReS_2 crystal marked by letter "d" is oriented such that the ReS_2 layer and the (001) planes are edge-on. The crystalline orientations are identified and confirmed by electron diffraction and Fourier transformation of the image as shown in the insets of Figure 1(a). The corresponding morphology and structure of the ReS_2 crystals following lithiation are shown in Figure 1(b). The final product is a mixture of fine Re clusters embedded in Li_2S nanocrystals (as identified by electron diffraction and high resolution electron microscopy (HREM) imaging as shown in the insets). After full lithiation, the elongation of the crystal along the [100] axis is about ~2.3% (expanded from ~129 nm to ~132 nm), while that along the [110] axis is about ~11% (expanded from ~54 nm to ~60 nm). Due to the stress induced during lithiation, the sample has also

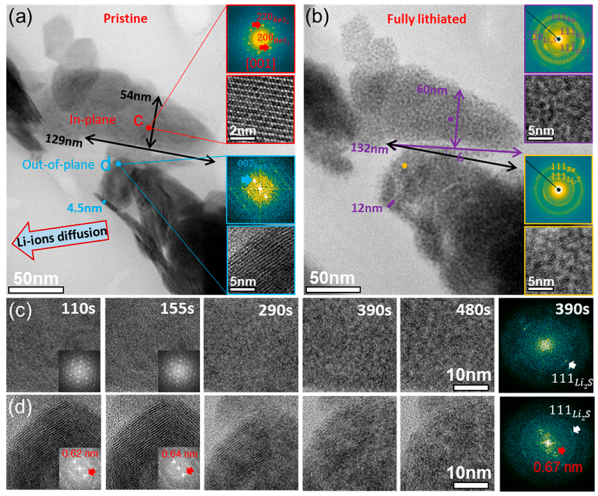

Figure 1. Anisotropic lithiation of ReS_2. (a) The pristine ReS_2 crystals with two crystallographic orientations: the area marked c is close to the [001] direction with diffraction pattern and HREM images as insets, while the area marked d is oriented such that the ReS_2 layer and the (001) planes are edge-on. (b) Lithiated ReS_2 showing changes in morphology and structure (as shown by electron diffraction) with significant volume expansion. (c) Time-labeled high-resolution TEM images of the [001] oriented ReS_2 in lithiation and the FFT spectrum of the images taken at 390 s. (d) Time-labeled high-resolution TEM images of the (001) plane edge-on ReS_2 in lithiation and the FFT spectrum of the images taken at 390 s. After full lithiation, a faint peak with ~0.67 nm can be found in the FFT spectrum obtained from area d. In comparison, there is no such spot seen from area c.

rotated ~6° counterclockwise, as marked in Figure 1(b). In comparison, the expansion along the [001] axis (perpendicular to the ReS_2 layers) after full lithiation is about ~167%, as shown in Figure S1(a,b). Evidently, the large difference in expansion along the out-of-plane direction compared to the in-plane direction confirms the anisotropy of lithiation. Meanwhile, the reaction dynamics also show large differences along the two directions. The direction of lithium-ion diffusion is shown in Figure 1(a). For the in-plane lithium-ion diffusion that is shown in Figure 1(c), the reaction is faster than that the out-of-plane diffusion that is shown in Figure 1(d). In particular, a uniform mixture of Re and Li_2S is formed in ~155 s (Figure 1(c)) for in-plane diffusion, whereas the reaction products form only after ~390 s (Figure 1(d)) for out-of-plane diffusion.

After lithiation, the reaction products (*i.e.*, Re metal clusters and Li_2S nanocrystals) have different structural characteristics along the two crystallographic orientations. When the lithiated products are observed along the out-of-plane direction, the Li_2S nanocrystals have uniform size and random orientations, as identified by the {111} diffraction ring in the diffraction pattern in the inset of Figure S1(c). However, when the lithiated products are observed along the in-plane direction (Figure S1(d)), the Li_2S nanocrystals are observed to possess a larger size with preferred orientations, as shown by the strong arcs marked by the red arrowheads in the diffraction pattern. In addition, the Re clusters generate a diffuse and wide ring in the diffraction pattern for both crystallographic directions, implying that the Re clusters have random orientations in both cases. However, by carefully investigating the spatial distribution of the Re clusters along the out-of-plane direction, the Re clusters are found to align in straight lines (as shown by the arrowheads in Figure S1(c)), which resembles the distribution

DOI: 10.1021/acsnano.8b02203
ACS Nano XXXX, XXX, XXX−XXX

of the ReS_2 layers in the pristine ReS_2 crystal (shown by arrowheads in the inset in Figure S1(a)). This relatively long-range and weak ordering in lithiated ReS_2 has clear signatures at the lithiation time of 390 s (Figure 1(d)). The Fourier transform spectrum of the HREM image taken along the out-of-plane direction after 390 s also shows faint and blurred spots corresponding to a *d*-spacing of 0.67 nm, as marked in the spectrum. In contrast, these spots are not observed along the in-plane direction (Figure 1(c)).

The directional sodiation of ReS_2 has also been studied. As shown in Figure 2(a,b) and Figure S2(a–d), the expansion

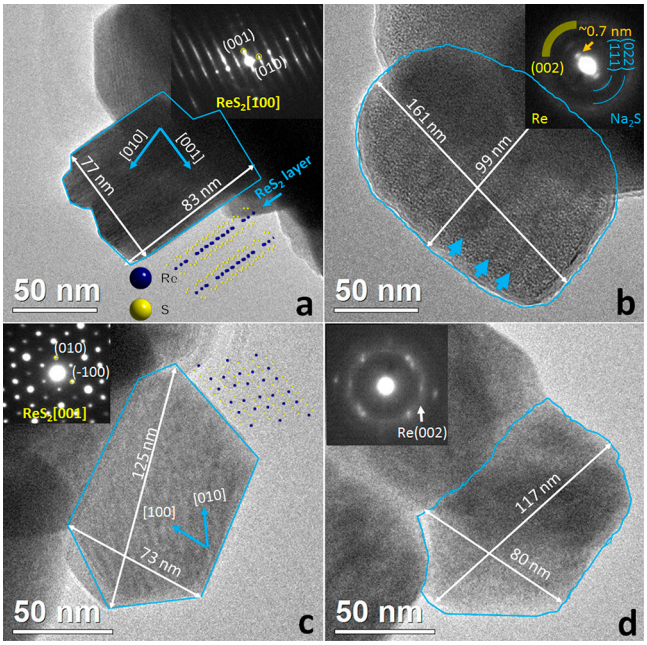

Figure 2. Anisotropic sodiation of ReS_2. (a) Pristine ReS_2 crystal in the out-of-plane direction. The orientation is identified by the electron diffraction as an inset. An illustration of ReS_2 structure and layers is also shown. (b) Lithiated ReS_2 in the out-of-plane direction, showing changes in morphology and structure (by the inset electron diffraction pattern). There is large expansion along the [001] direction and diffraction spots with a *d*-spacing of ~0.7 nm, resulting from the modulated structure of Re clusters and Na_2S lamellas. (c) Pristine ReS_2 crystal in the in-plane direction. The orientation is identified by the electron diffraction as an inset. An illustration of ReS_2 structure and layers is also shown. (d) Lithiated ReS_2 in the in-plane direction, showing changes in morphology and structure (by the inset electron diffraction pattern). There are several bright diffraction spots corresponding to Na_2S, which implies that Na_2S has a preferred orientation along the in-plane direction.

of a ReS_2 crystal oriented close to the [100] axis after sodiation (Figure 2b) is measured and compared to that before sodiation (Figure 2a). The crystal expanded significantly along the [001] axis, which is the normal to the ReS_2 layers, namely, from ~77 nm to ~161 nm with ~109% elongation in the crystallographic orientation perpendicular to the ReS_2 layers. In comparison, there is only ~19% elongation along the [010] axis. From an in-plane oriented ReS_2 crystal (Figure 2c), the elongation along the [100] axis is ~10% (expanded from ~73 nm to ~80 nm). With a ReS_2 layer (*i.e.*, the (001) lattice plane) as the reference plane, the out-of-plane expansion is almost 10 times larger than that of in-plane expansion, thus confirming strong anisotropy in sodiation.

A similar modulated structure appears in sodiated ReS_2, as evidenced by the spots with a *d*-spacing of ~0.7 nm marked by an arrowhead in the diffraction pattern in the inset of Figure 2(b). There are also many lines with faint contrast, as marked by the red arrowheads in Figure 2(b), which may be caused by the alignment of the Re clusters in the fully sodiated sample. The modulated structure is thus likely originated from the intergrowth of Na_2S thin crystals and Re clusters. Meanwhile, the Na_2S crystal formed after sodiation shows different character along the out-of-plane direction and the in-plane direction. When the sodiated ReS_2 is investigated in the in-plane direction by electron diffraction, several diffraction spots for Na_2S are observed, implying that the Na_2S crystals are large and have preferred orientation. Similar to lithiated ReS_2, sodiated ReS_2 has small crystal size and random orientation when viewed along the out-of-plane direction (as shown by the uniform ring of Na_2S in the diffraction pattern).

The anisotropic structure of ReS_2 has led to a preference in the direction of lithiation/sodiation, which leads to an anisotropic structure after lithiation/sodiation. Figure 3 illustrates the 3D

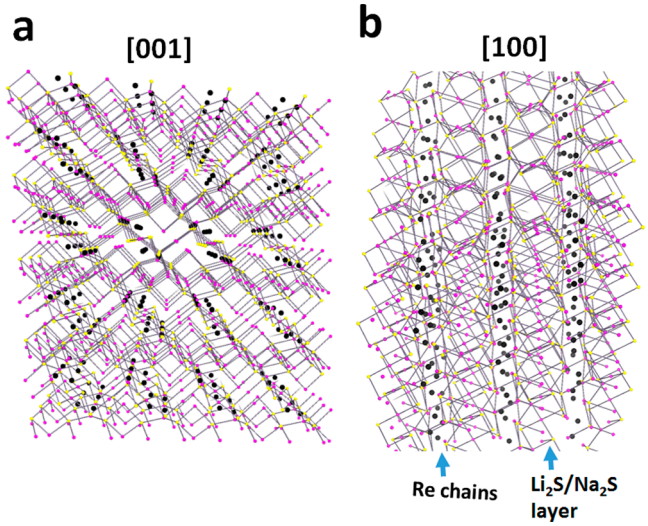

Figure 3. Illustration of the lithiated/sodiated ReS_2 with modulated structure with Re clusters and Li_2S/Na_2S lamellas. (a) In-plane direction (along the [001] direction) and (b) out-of-plane direction. Along the in-plane direction, the product is covered by Li_2S/Na_2S layers, which hinders transport of both electron and ions. In the out-of-plane direction (b), Re cluster chains form a highly conductive pathway for electrons. The gap along this direction is also large and thus provides a fast diffusion pathway for ions.

structure of lithiated/sodiated ReS_2. A layered structure has been maintained with spatial modulation of the Re clusters and Li_2S/Na_2S layers along the out-of-plane direction. For lithiated/sodiated ReS_2, electrical conductivity along the in-plane direction is higher due to the chains formed by the Re metal clusters. Along the in-plane direction, the chains formed by conductive Re clusters facilitate charge transport. On the other hand, along the out-of-plane direction, the continuous Li_2S/Na_2S layer with low electrical conductivity will impede charge transport.

Further insight into the reaction mechanism of ReS_2 lithiation and sodiation is provided by DFT calculations that are correlated with the *in situ* TEM observations. The reaction begins with intercalation of lithium/sodium ions and is followed by a conversion reaction leading to phase separation and

DOI: 10.1021/acsnano.8b02203
ACS Nano XXXX, XXX, XXX–XXX

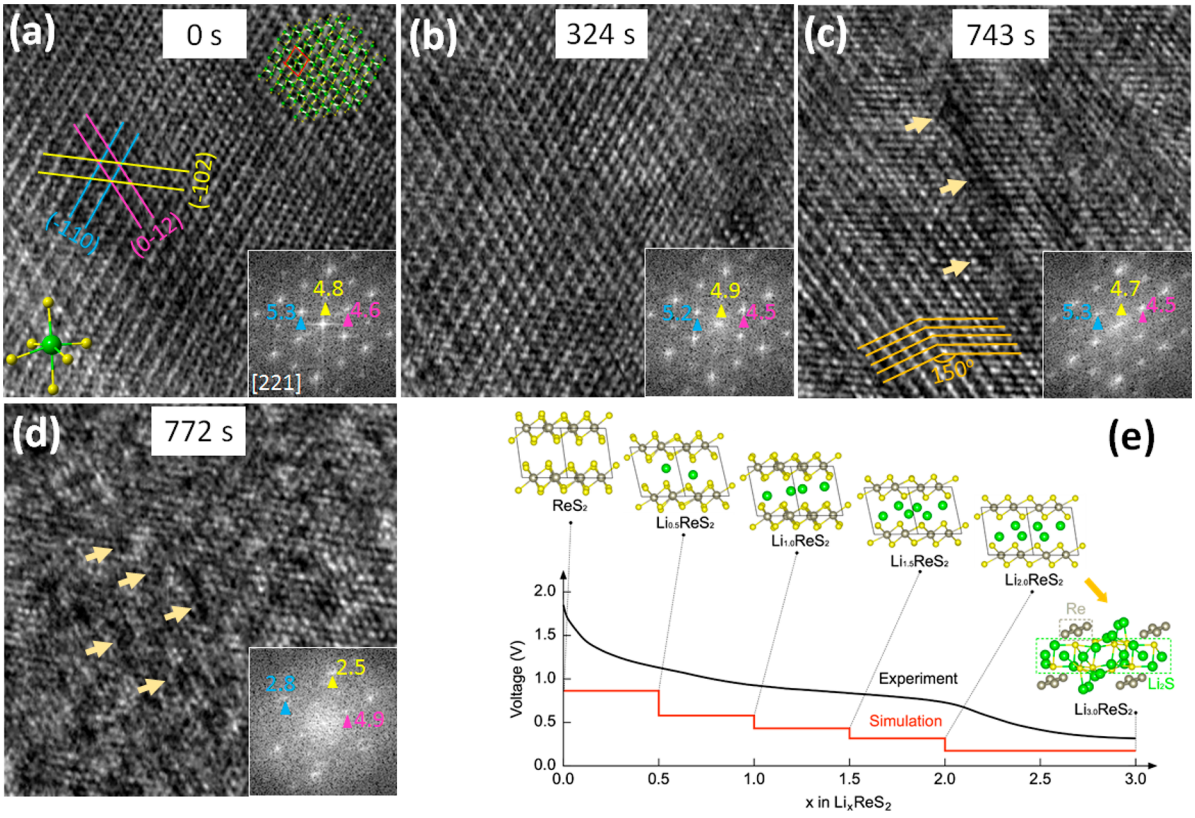

Figure 4. Evolution of the structure of ReS_2 in lithiation studied by HREM images. (a–d) Time-resolved HREM images of the ReS_2 with lithiation times of 0 to 772 s marked in the picture. The lattice expansion and distortion are seen with the lithiation process and extrusion of Re clusters (dark contrast dots in the images as marked by light yellow arrowheads). (e) Calculated lithiation process by DFT. In lithiation, four intermediate and intercalated phases are identified by DFT. When the number of lithium ions is larger than 2 per unit formula, phase separation due to a conversion reaction occurs.

formation of fine Re metal nanoparticles and Li_2S/Na_2S nanocrystals. As shown in Figure S4, the time-resolved electron diffraction patterns during lithiation provide evidence of the phase evolution. Since pristine ReS_2 has a 1T-type structure, we do not observe the 2H-to-1T phase transformation that is well-known for MoS_2. Instead, as shown in Figure S5, the *d*-spacing of the lithiated ReS_2 structures became large when the amount of intercalated Li-ions increases, in agreement with DFT simulations.

The microstructure evolution during ReS_2 lithiation has also been characterized by the *in situ* high-resolution TEM image in Figure 4 and Figures S6 and S7. The upper inset in Figure 4(a) shows the initial atomic structure of a crystalline ReS_2 nanosheet along the [221] zone axis. One brighter spot represents a cluster of one Re in the center of the octahedron formed by six S. Planes of (−110), (0−12), and (−102) can be characterized and are labeled with blue, yellow, and pink arrowheads, respectively. The lower inset is the corresponding fast Fourier transform (FFT) image. While lattice expansion is observed following lithiation, planar distortion and collapse of the original ReS_2 lattice are also observed along with the extrusion of Re atoms and formation of metal Re clusters and Li_2S crystals. The correlation between the Re cluster extrusion and ReS_2 lattice distortion as well as the occurrence of planar defects is shown in Figure S7. With the insertion of Li-ions, the location where a Re cluster forms (as indicated by the arrowheads in Figure 4c) corresponds to the ReS_2 (−110) lattice plane distortion, as shown in a Fourier filtered image (Figure S7d−1) showing only the (−110) lattice plane. With the further insertion of lithium ions, more Re clusters are extruded from the ReS_2 lattice, which causes the generation of lattice distortion as shown in Figure S7(e−h). The observation confirms that the extrusion of the metal clusters from the ReS_2 parent lattice causes local stress/strain that is released by generation of local lattice defects. The accumulation of this strain upon further insertion of Li-ions prompts phase transformation and separation from ReS_2 to Re and Li_2S. There must be a critical size of the metal cluster, above which the lamella structure becomes unstable. In our DFT calculation, such a critical size remains difficult to predict since a prohibitively long computing time is needed when the size of the clusters become large, *i.e.*, ∼tens of nanometers.

Differences are observed in the microstructural evolutions between lithiation and sodiation. In lithiation (Figures S4−S7), the transition from intercalated to conversion reaction is smoother with many intermediate phases compared to sodiation (Figures S8 and S9). According to the volume predictions from DFT calculations, the volume expansions in sodiation are significantly larger than that in lithiation (Figure S10), especially at the last stage of sodiation/lithiation. Larger volume expansion causes increased strain and therefore higher crack density for sodiated particles, leading to a less stable sodiation behavior. Meanwhile, the crystallinity of Li_2S is better than Na_2S in the final reaction products. Specifically, while Li_2S signal can be detected in electron diffraction after lithiation, the diffraction ring of Na_2S is more blurred and diffuse after sodiation.

By DFT calculations (Figures S11 and S12), several intermediate lithium-ion intercalated phases are predicted and

DOI: 10.1021/acsnano.8b02203
ACS Nano XXXX, XXX, XXX−XXX

shown in Figure 4(e). The calculated voltage profile (Figure 4(e)) is compared to the experimental voltage curve measured by Zhang *et al.*[9] Similar results are obtained for the sodiation of ReS_2 as shown in Figure S13. During the lithiation of ReS_2, lithium-ions intercalated into the ReS_2 lattice form an intercalated structure when the number of lithium-ions is less than 2 per unit structure formula. The threshold of Li content above which the conversion reaction will occur is 2 per unit formula (*i.e.*, Li_2ReS_2), while the corresponding voltage is about ~0.2 V. During sodiation of ReS_2, the intercalation reaction lasts only until the number of intercalated Na-ions is less than 1 per unit structure formula. Meanwhile, the threshold of Na content is 1 per unit formula (*i.e.*, $NaReS_2$) at a voltage of ~0.58 V. Above the thresholds, Re ions start to be reduced to their metal states and the conversion reaction occurs. As phase separation in a conversion reaction will introduce large volumetric expansion and lattice distortion, reversibility of the reaction is greatly reduced. After exceeding this intercalation threshold, conversion reaction dominates the phase transformation for both lithiation and sodiation. Although the phase transformation from ReS_2 to Re and Li_2S/Na_2S caused large volumetric expansion and lattice distortion, the intercalated intermediate phases make it a smooth transition, generating anisotropic products similar to the original anisotropic structure of ReS_2. As anisotropy in the lithiated/sodiated ReS_2 has been faithfully inherited from the original anisotropic ReS_2, its impact on battery properties (especially rate capability and cycling stability) lasts many cycles. It is thus tempting to suggest to align the anisotropic crystals with their high electrical and ionic conductivity along the direction of lithiation/sodiation to improve the electrochemical performance of rechargeable batteries. This anisotropy or tailoring of the crystallography and morphological texture is likely to be an important design parameter for the high performance in future generation batteries. Although it is still in progress, there are several methods for fabricating 2D materials with vertical orientation onto a substrate. For example, with 3D graphene foam as a template, chemical vapor deposition can be used to synthesize vertical ReS_2 nanowalls.[9] The vertical alignment of two-dimensional Mxene has also been achieved by mechanical shearing of a discotic lamellar liquid-crystal phase.[21] In addition, vertically aligned reduced graphene oxide electrodes have been prepared using simple hand-rolling and cutting processes.[22]

CONCLUSIONS

The reaction mechanisms of ReS_2 during lithiation and sodiation have been studied by *in situ* TEM and correlated DFT calculations. The anisotropic structure of ReS_2 leads to anisotropic lithiation and sodiation along the out-of-plane and in-plane directions. In the in-plane direction, modulated metal Re clusters and Li_2S/Na_2S form a lamellar structure that enables faster interfacial Li/Na insertion/extraction kinetics. In the out-of-plane direction, the Li_2S/Na_2S layers block the transport of electrons and ions, resulting in slow kinetics. We also observe that Re metal clusters cause local ReS_2 lattice distortions that prompt phase transformation and separation. Overall, we believe this study provides insight into the application and design of anisotropic layered crystals as electrodes in high-performance rechargeable batteries.

METHODS/EXPERIMENTAL

ReS_2 Dispersion Preparation. To fully exploit and understand the properties of 2D ReS_2, a scalable production method is required. Previous work has been done *via* micromechanical[11,14,15,23] and chemical exfoliation[24] approaches. Although micromechanical exfoliation yields high-quality materials, it is not suitable for scalable applications due to exceptionally low yields and throughput. As a scalable approach, chemical exfoliation can produce larger quantities of 2D materials. However, this process results in a phase transition during the exfoliation process that requires post processing (*e.g.*, high-temperature annealing) to attempt to recover the original crystal structure. Alternatively, liquid-phase exfoliation *via* ultrasonication is a well-established approach for scalable exfoliation of 2D nanomaterials without chemical modification.[25−27] In our synthesis method, 30 mg of ReS_2 powder (American Elements) was placed in a 50 mL conical tube with 10 mL of ethanol and 5 mL of deionized water. The mixture was ultrasonicated (Fisher Scientific model 500 sonic dismembrator) with a 0.125 in. diameter tip for 2 h at a power level of ~50 W in an ice bath (pulsed 2 s on and 1 s off to avoid solvent evaporation). As-prepared ReS_2 dispersions were then centrifuged at 1000 rpm for 10 min to remove unexfoliated ReS_2 powder (Avanti J-26 XP, Beckman Coulter). Following the centrifugation, the supernatant was carefully decanted for the experiments.

Characterization. TEM observation was performed by a field-emission JEOL JEM-2100F and JEM-ARM300F TEM.

***In Situ* TEM.** A Nanofactory *in situ* holder was used to build an open half-cell inside the TEM column. There is a dual-probe design in the holder. One probe uses a Au rod to load sample (with ReS_2 attached to its tip). Another, tungsten (W) probe is moveable inside the TEM column. It is driven by a piezo-motor capable of 3D positioning with a step-size of 1 nm. Inside an Ar-filled glovebox, we took the W probe tip and scratched it on a Li metal strip and then affixed it on the TEM holder. With an airtight cover, the TEM holder was transferred and inserted into the TEM column with limited exposure to air (estimated about ~10 s). A layer of lithium oxide was grown on the surface of Li metal during transportation and acted as a solid electrolyte. We applied a −2.5 V potential on the Nanofactory holder to initialize lithiation and sodiation. We performed *in situ* TEM on many ReS_2 particles to ensure the observation of anisotropy is a common phenomenon that can be repeatedly observed. One of the results is shown in Figure S14 and Video S5. As for the *in situ* TEM experiments, the probe current measured by a Faraday holder is ~3600 pA. There are thus about ~2.25×10^{10} electrons per second ($e^- s^{-1}$) in the probe. The illumination area is half of the screen (125 cm^2) at a magnification of 500 000, which is 5×10^6 $Å^{-2}$ as the area on the specimen. Thus, the dose rate in the *in situ* experiments is about ~4500 $e^- Å^{-2} s^{-1}$. Control experiments on ReS_2 crystals were performed by applying an electron beam at a similar dose rate without connecting to the W probe (with Li_2O/Li) and no external potential. As shown in Figure S15, the ReS_2 is stable when exposed only to the electron beam.

First-Principles Calculations. First-principles DFT calculations were performed *via* the Vienna Ab-initio Simulation Package (VASP)[28−30] with projector-augmented wave (PAW) potentials.[31] For the exchange−correlation functional, we used the generalized gradient approximation (GGA) of Perdew−Becke−Ernzerhof (PBE).[32] We used two different sets of parameters: one for lower energy configuration sampling and the other for accurate total energy determination. For the coarse energy sampling calculations, a plane-wave basis set with a cutoff energy of 300 eV and Γ-centered *k*-meshes with a density of 2000 *k*-points per reciprocal atom were used. The accurate total energy calculations were performed with a plane-wave basis set cutoff energy of 520 eV and Γ-centered *k*-meshes with a density of 8000 *k*-points per reciprocal atom.

To search for the intermediate phases through the Li(Na)−ReS_2 reaction, the nonequilibrium phase search method (NEPS)[33−35] was applied by exploring geometrically distinct Li(Na)/vacancy configurations on possible insertion sites of the ReS_2 structure (Figure S10) at different compositions (Li/vacancy ratios). First, we made an assumption that Li/Na diffusion in transition metal sulfides is significantly faster than transition metal and sulfur ions during the lithiation/sodiation reactions, as observed in previous studies.[36] As a result, the Li(Na) ion(s) can take any energetically favored unoccupied site(s) while the migrations of transition metal and sulfur ions are constrained,

DOI: 10.1021/acsnano.8b02203
ACS Nano XXXX, XXX, XXX−XXX

therefore enabling the nonequilibrium lithiation process. The method proceeds as follows: (i) identify all possible insertion sites in the original ReS_2 structure using MINT.[37,38] ReS_2 adopts a triclinic structure with unoccupied octahedral (O_h) and tetrahedral (T_d) sites, as shown in Figure S10. A supercell containing 2 Re^{4+} and 4 S^{2-} ions was built that has 12 total empty sites in which Li(Na) ions can insert. (ii) Generate all symmetrically distinct configurations with Enum.[39,40] for a series of compositions $Li(Na)_x\square_{3-x}ReS_2$ ($0 < x < 2$, $\square$ denoting vacancy). (iii) Sample total energies of all configurations with coarse settings described in the previous section. (iv) For the specific composition, corresponding structures were ranked by their total energies, and the three lowest energy structures were further relaxed in DFT with more strict settings. Formation energies of selected structures were then calculated according to following reaction: $ReS_2 + xLi(Na) \rightarrow Li(Na)_xReS_2$. (v) Build the lithiation/sodiation convex hull using the formation energies, and the composition points on the hull were determined to be the nonequilibrium intermediate phases.

Voltage Calculations. The average lithiation/sodiation voltage (relative to Li/Li^+ and Na/Na^+) was computed using the negative of the reaction free energy per A = Li/Na added, as shown in eq 1:[41]

$$V = \frac{\Delta G_f}{F\Delta N_A} \quad (1)$$

where F is the Faraday constant, ΔN_A is the amount of Li/Na added/removed, and ΔG_f is the (molar) change in free energy of the reaction. Considering a two-phase reaction between A_xReS_2 and A_yReS_2: $A_xReS_2 + (y - x)A \rightarrow A_yReS_2$, ΔG_f can be approximated by the total internal energies from DFT calculations neglecting the entropic contributions (0 K),

$$\Delta E = E(A_yReS_2) - E(A_xReS_2) - (y - x)E(A_{metal}) \quad (2)$$

where $E(A_xReS_2)$ and $E(A_yReS_2)$ are the DFT energies at the respective compositions. The neglect of entropic contributions means that the lithiation voltage profiles will follow the $T = 0$ K ground-state convex hull and consist of a series of constant voltage steps along the two-phase regions of the convex hull, separated by discontinuities that indicate the single-phase compounds on the hull. It is worth mentioning here that, in practice, lithiation/delithiation does not necessarily proceed through two-phase reactions. Thus, the calculated $T = 0$ K voltage profiles should be viewed as an approximation to the actual voltage profiles.[42] At finite temperatures (*e.g.*, room temperature), the voltage drops in the profile become more rounded, due to entropic effects. For simplicity, the voltages were calculated at a temperature of 0 K, and thus the voltage drops in the simulated voltage profiles exhibit abrupt steps. This behavior is smoother when finite temperature effects are included.[43]

ASSOCIATED CONTENT

Supporting Information

The Supporting Information is available free of charge on the ACS Publications website at DOI: 10.1021/acsnano.8b02203.

Supplementary movie (AVI)
Supplementary movie (AVI)
Supplementary movie (AVI)
Supplementary figures (PDF)
Supplementary movie (AVI)
Supplementary movie (AVI)

AUTHOR INFORMATION

Corresponding Authors

*E-mail: jinsong-wu@northwestern.edu.
*E-mail: v-dravid@northwestern.edu.

ORCID

Yaobin Xu: 0000-0002-9945-3514
Zhenpeng Yao: 0000-0001-8286-8257
Joohoon Kang: 0000-0002-6578-2547
Xiaolong Liu: 0000-0002-6186-5257
Chris Wolverton: 0000-0003-2248-474X
Mark C. Hersam: 0000-0003-4120-1426
Jinsong Wu: 0000-0002-7305-7927
Vinayak P. Dravid: 0000-0002-6007-3063

Present Address

[¶]Department of Chemistry and Chemical Biology, Harvard University, 12 Oxford Street, Cambridge, Massachusetts 02138, United States.

Notes

The authors declare no competing financial interest.

ACKNOWLEDGMENTS

Q.L. and Y.X. contributed equally to this work. Q.L., Y.X., and J.W. (*in situ* TEM and interpretation), Z.Y. and C.W. (DFT calculations), X.L. and M.C.H. (battery measurements), and V.P.D. (TEM interpretation) were supported as part of the Center for Electrochemical Energy Science, an Energy Frontier Research Center funded by the U.S. Department of Energy (DOE), Office of Science, Basic Energy Sciences, under Award No. DEAC02-06CH11357. J.W. and V.P.D. were also supported by the Samsung Advanced Institute of Technology (SAIT)'s Global Research Outreach (GRO) Program and the Initiative for Sustainability and Energy at Northwestern (ISEN). Q.L. gratefully acknowledges the support of the National Natural Science Foundation of China (Grant No. 51702207) as well. J.K. acknowledges support from the National Science Foundation (DMR-1505849) for solution processing of ReS_2. Portions of this work were performed in the NU*ANCE* Center at Northwestern University, using the EPIC facility, which receives support from the Soft and Hybrid Nanotechnology Experimental (SHyNE) Resource (NSF NNCI-1542205); the MRSEC program (NSF DMR-1720139) at the Materials Research Center; the International Institute for Nanotechnology (IIN); the Keck Foundation; and the State of Illinois, through the IIN. We gratefully acknowledge computing resources from (1) the National Energy Research Scientific Computing Center, a DOE Office of Science User Facility supported by the Office of Science of the U.S. Department of Energy under Contract DE-AC02-05CH11231, and (2) Blues, a high-performance computing cluster operated by the Laboratory Computing Resource Center at Argonne National Laboratory.

REFERENCES

(1) Bousa, M.; Laskova, B.; Zukalova, M.; Prochazka, J.; Chou, A.; Kavan, L. Polycrystalline TiO_2 Anatase with a Large Proportion of Crystal Facets (001): Lithium Insertion Electrochemistry. *J. Electrochem. Soc.* **2010**, *157*, A1108−A1112.

(2) Hengerer, R.; Kavan, L.; Krtil, P.; Gratzel, M. Orientation Dependence of Charge-Transfer Processes on TiO_2 (anatase) Single Crystals. *J. Electrochem. Soc.* **2000**, *147*, 1467−1472.

(3) Auer, A.; Portenkirchner, E.; Gotsch, T.; Valero-Vidal, C.; Penner, S.; Kunze-Liebhauser, J. Preferentially Oriented TiO_2 Nanotubes as Anode Material for Li-Ion Batteries: Insight into Li-Ion Storage and Lithiation Kinetics. *ACS Appl. Mater. Interfaces* **2017**, *9*, 36828−36836.

(4) Pumera, M.; Sofer, Z.; Ambrosi, A. Layered Transition Metal Dichalcogenides for Electrochemical Energy Generation and Storage. *J. Mater. Chem. A* **2014**, *2*, 8981−8987.

DOI: 10.1021/acsnano.8b02203
ACS Nano XXXX, XXX, XXX−XXX

(5) Stephenson, T.; Li, Z.; Olsen, B.; Mitlin, D. Lithium Ion Battery Applications of Molybdenum Disulfide (MoS_2) Nanocomposites. *Energy Environ. Sci.* **2014**, *7*, 209−231.
(6) Huang, G.; Chen, T.; Chen, W.; Wang, Z.; Chang, K.; Ma, L.; Huang, F.; Chen, D.; Lee, J. Graphene-Like MoS_2/Graphene Composites: Cationic Surfactant-Assisted Hydrothermal Synthesis and Electrochemical Reversible Storage of Lithium. *Small* **2013**, *9*, 3693−3703.
(7) Sahu, T. S.; Li, Q.; Wu, J.; Dravid, V. P.; Mitra, S. Exfoliated MoS_2 Nanosheets Confined in 3-D Hierarchical Carbon Nanotube@ Graphene Architecture with Superior Sodium-Ion Storage. *J. Mater. Chem. A* **2017**, *5*, 355−363.
(8) Li, Q.; Yao, Z.; Wu, J.; Mitra, S.; Hao, S.; Sahu, T. S.; Li, Y.; Wolverton, C.; Dravid, V. P. Intermediate Phases in Sodium Intercalation into MoS_2 Nanosheets and Their Implications for Sodium-Ion Batteries. *Nano Energy* **2017**, *38*, 342−349.
(9) Zhang, Q.; Tan, S. J.; Mendes, R. G.; Sun, Z. T.; Chen, Y. T.; Kong, X.; Xue, Y. H.; Rummeli, M. H.; Wu, X. J.; Chen, S. L.; Fu, L. Extremely Weak van der Waals Coupling in Vertical ReS_2 Nanowalls for High-Current-Density Lithium-Ion Batteries. *Adv. Mater.* **2016**, *28*, 2616−2623.
(10) Gao, J.; Li, L.; Tan, J. W.; Sun, H.; Li, B. C.; Idrobo, J. C.; Singh, C. V.; Lu, T. M.; Koratkar, N. Vertically Oriented Arrays of ReS_2 Nanosheets for Electrochemical Energy Storage and Electrocatalysis. *Nano Lett.* **2016**, *16*, 3780−3787.
(11) Chenet, D.; Aslan, O.; Huang, P. Y.; Fan, C.; van der Zande, A. M.; Heinz, T. F.; Hone, J. C. In-Plane Anisotropy in Mono- and Few-Layer ReS_2 Probed by Raman Spectroscopy and Scanning Transmission Electron Microscopy. *Nano Lett.* **2015**, *15*, 5667−5672.
(12) Tongay, S.; Zhou, J.; Ataca, C.; Lo, K.; Matthews, T. S.; Li, J. B.; Grossman, J. C.; Wu, J. Q. Thermally Driven Crossover from Indirect toward Direct Bandgap in 2D Semiconductors: $MoSe_2$ *versus* MoS_2. *Nano Lett.* **2012**, *12*, 5576−5580.
(13) Jin, W.; Yeh, P.; Zaki, N.; Zhang, D. T.; Sadowski, J. T.; Al-Mahboob, A.; van der Zande, A. M.; Chenet, D. A.; Dadap, J. I.; Herman, I. P.; Sutter, P.; Hone, J.; Osgood, R. M. Direct Measurement of the Thickness-Dependent Electronic Band Structure of MoS_2 Using Angle-Resolved Photoemission Spectroscopy. *Phys. Rev. Lett.* **2013**, *111*, 106801.
(14) Liu, E. F.; Fu, Y. J.; Wang, Y. J.; Feng, Y. Q.; Liu, H. M.; Wan, X. G.; Zhou, W.; Wang, B. G.; Shao, L. B.; Ho, C. H.; Huang, Y. S.; Cao, Z. Y.; Wang, L. G.; Li, A. D.; Zeng, J. W.; Song, F. Q.; Wang, X. R.; Shi, Y.; Yuan, H. T.; Hwang, H. Y.; et al. Integrated Digital Inverters Based on Two-Dimensional Anisotropic ReS_2 Field-Effect Transistors. *Nat. Commun.* **2015**, *6*, 6991.
(15) Tongay, S.; Sahin, H.; Ko, C.; Luce, A.; Fan, W.; Liu, K.; Zhou, J.; Huang, Y. S.; Ho, C. H.; Yan, J. Y.; Ogletree, D. F.; Aloni, S.; Ji, J.; Li, S. S.; Li, J. B.; Peeters, F. M.; Wu, J. Q. Monolayer Behaviour in Bulk ReS_2 due to Electronic and Vibrational Decoupling. *Nat. Commun.* **2014**, *5*, 3252.
(16) Qi, F.; Chen, Y. F.; Zheng, B. J.; He, J. R.; Li, Q.; Wang, X. G.; Lin, J.; Zhou, J. H.; Yu, B.; Li, P. J.; Zhang, W. L. Hierarchical Architecture of ReS_2/rGO Composites with Enhanced Electrochemical Properties for Lithium-Ion Batteries. *Appl. Surf. Sci.* **2017**, *413*, 123−128.
(17) Qi, F.; He, J. R.; Chen, Y. F.; Zheng, B. J.; Li, Q.; Wang, X. Q.; Yu, B.; Lin, J.; Zhou, J. H.; Li, P. J.; Zhang, W. L.; Li, Y. R. Few-Layered ReS_2 Nanosheets Grown on Carbon Nanotubes: A Highly Efficient Anode for High-Performance Lithium-Ion Batteries. *Chem. Eng. J.* **2017**, *315*, 10−17.
(18) Li, Q.; Wu, J.; Yao, Z.; Xu, Y.; Thackeray, M. M.; Wolverton, C.; Dravid, V. P. Dynamic Imaging of Metastable Reaction Pathways in Lithiated Cobalt Oxide Electrodes. *Nano Energy* **2018**, *44*, 15−22.
(19) Liu, H.; Li, Q.; Yao, Z.; Li, L.; Li, Y.; Wolverton, C.; Hersam, M. C.; Wu, J.; Dravid, V. P. Origin of Fracture-Resistance to Large Volume Change in Cu-Substituted Co_3O_4 Electrodes. *Adv. Mater.* **2018**, *30*, 1704851.
(20) Li, Q.; Liu, H.; Yao, Z.; Cheng, J. P.; Li, T. H.; Li, Y.; Wolverton, C.; Wu, J.; Dravid, V. P. Electrochemistry of Selenium with Sodium and Lithium: Kinetics and Reaction Mechanism. *ACS Nano* **2016**, *10*, 8788−8795.
(21) Xia, Y.; Mathis, T. S.; Zhao, M. Q.; Anasori, B.; Dang, A.; Zhou, Z. H.; Cho, H.; Gogotsi, Y.; Yang, S. Thickness-Independent Capacitance of Vertically Aligned Liquid-Crystalline MXenes. *Nature* **2018**, *557*, 409−412.
(22) Yoon, Y.; Lee, K.; Kwon, S.; Seo, S.; Yoo, H.; Kim, S.; Shin, Y.; Park, Y.; Kim, D.; Choi, J. Y.; Lee, H. Vertical Alignments of Graphene Sheets Spatially and Densely Piled for Fast Ion Diffusion in Compact Supercapacitors. *ACS Nano* **2014**, *8*, 4850−4890.
(23) Lin, Y. C.; Komsa, H. P.; Yeh, C. H.; Bjorkman, T.; Liang, Z. Y.; Ho, C. H.; Huang, Y. S.; Chiu, P. W.; Krasheninnikov, A. V.; Suenaga, K. Single-Layer ReS_2: Two-Dimensional Semiconductor with Tunable In-Plane Anisotropy. *ACS Nano* **2015**, *9*, 11249−11257.
(24) Fujita, T.; Ito, Y.; Tan, Y. W.; Yamaguchi, H.; Hojo, D.; Hirata, A.; Voiry, D.; Chhowalla, M.; Chen, M. W. Chemically Exfoliated ReS_2 Nanosheets. *Nanoscale* **2014**, *6*, 12458−12462.
(25) Green, A. A.; Duch, M. C.; Hersam, M. C. Isolation of Single-Walled Carbon Nanotube Enantiomers by Density Differentiation. *Nano Res.* **2009**, *2*, 69−77.
(26) Kang, J.; Sangwan, V. K.; Wood, J. D.; Hersam, M. C. Solution-Based Processing of Monodisperse Two-Dimensional Nanomaterials. *Acc. Chem. Res.* **2017**, *50*, 943−951.
(27) Kang, J.; Sangwan, V. K.; Wood, J. D.; Liu, X.; Balla, I.; Lam, D.; Hersam, M. C. Layer-by-Layer Sorting of Rhenium Disulfide *via* High-Density Isopycnic Density Gradient Ultracentrifugation. *Nano Lett.* **2016**, *16*, 7216−7223.
(28) Kresse, G.; Hafner, J. Ab Initio Molecular Dynamics for Liquid Metals. *Phys. Rev. B: Condens. Matter Mater. Phys.* **1993**, *47*, 558−561.
(29) Kresse, G.; Hafner, J. Ab-Initio Molecular-dynamics Simulation of The Liquid-Metal Amophous-Semiconductor Transition in Germanuim. *Phys. Rev. B: Condens. Matter Mater. Phys.* **1994**, *49*, 14251−14269.
(30) Kresse, G.; Furthmüller, J. Efficient Iterative Schemes for Ab Initio Total-energy Calculations Using a Plane-Wave Basis Set. *Phys. Rev. B: Condens. Matter Mater. Phys.* **1996**, *54*, 11169−11186.
(31) Blochl, P. E. Projector Augmented-Wave Methold. *Phys. Rev. B: Condens. Matter Mater. Phys.* **1994**, *50*, 17953−17979.
(32) Perdew, J. P.; Ernzerhof, M.; Burke, K. Rationale for Mixing Exact Exchange with Density Functional Approximations. *J. Chem. Phys.* **1996**, *105*, 9982−9985.
(33) Yao, Z.; Kim, S.; Aykol, M.; Li, Q.; Wu, J.; He, J.; Wolverton, C. Revealing the Conversion Mechanism of Transition Metal Oxide Electrodes during Lithiation from First-Principles. *Chem. Mater.* **2017**, *29*, 9011−9022.
(34) Yao, Z.; Kim, S.; He, J.; Hegde, V. I.; Wolverton, C. Interplay of Cation and Anion Redox in $Li_4Mn_2O_5$ Cathode Material and Prediction of Improved $Li_4(Mn,M)_2O_5$ Electrodes for Li-Ion Batteries. *Sci. Adv.* **2018**, *4*, eaao6754.
(35) Zhan, C.; Yao, Z.; Lu, J.; Ma, L.; Maroni, V. A.; Li, L.; Lee, E.; Alp, E. E.; Wu, T.; Wen, J.; Ren, Y.; Johnson, C.; Thackeray, M. M.; Chan, M. K. Y.; Wolverton, C.; Amine, K. Enabling the High Capacity of Lithium-Rich Anti-Fluorite Lithium Iron Oxide by Simultaneous Anionic and Cationic Redox. *Nat. Energy* **2017**, *2*, 963−971.
(36) He, K.; Yao, Z.; Hwang, S.; Li, N.; Sun, K.; Gan, H.; Du, Y.; Zhang, H.; Wolverton, C.; Su, D. Kinetically-Driven Phase Transformation during Lithiation in Copper Sulfide Nanoflakes. *Nano Lett.* **2017**, *17*, 5726−5733.
(37) Ward, L.; Michel, K. *Materials/Mint: Initial Release*; Zenodo, 2016.
(38) Michel, K. J.; Wolverton, C. Symmetry Building Monte Carlo-Based Crystal Structure Prediction. *Comput. Phys. Commun.* **2014**, *185*, 1389−1393.
(39) Hart, G. L. W.; Forcade, R. W. Algorithm for Generating Derivative Structures. *Phys. Rev. B: Condens. Matter Mater. Phys.* **2008**, *77*, 224115−224126.
(40) Hart, G. L. W.; Nelson, L. J.; Forcade, R. W. Generating Derivative Structures at a Fixed Concentration. *Comput. Mater. Sci.* **2012**, *59*, 101−107.

DOI: 10.1021/acsnano.8b02203
ACS Nano XXXX, XXX, XXX−XXX

(41) Aydinol, M. K.; Kohan, A. F.; Ceder, G.; Cho, K.; Joannopoulos, J. Ab Initio Study of Lithium Intercalation in Metal Oxides and Metal Dichalcogenides. *Phys. Rev. B: Condens. Matter Mater. Phys.* **1997**, *56*, 1354−1365.
(42) Chan, M. K. Y.; Wolverton, C.; Greeley, J. P. First Principles Simulations of the Electrochemical Lithiation and Delithiation of Faceted Crystalline Silicon. *J. Am. Chem. Soc.* **2012**, *134*, 14362−14374.
(43) Wolverton, C.; Zunger, A. First-Principles Prediction of Vacancy Order-Disorder and Intercalation Battery Voltages in $LixCoO_2$. *Phys. Rev. Lett.* **1998**, *81*, 606−609.

DOI: 10.1021/acsnano.8b02203
ACS Nano XXXX, XXX, XXX−XXX